Research Article | Vol. 32, No. 21 / 7 Oct 2024 / Optics Express 36632
Optics EXPRESS

Direct laser write lithography for high optical quality electrowetting prisms

EDUARDO J. MISCLES,[1] MO ZOHRABI,[2] JULIET T. GOPINATH,[2,3,4,*] AND VICTOR M. BRIGHT[1]

[1]Department of Mechanical Engineering, University of Colorado Boulder, Boulder, Colorado 80309, USA
[2]Department of Electrical, Computer, and Energy Engineering, University of Colorado Boulder, Boulder, Colorado 80309, USA
[3]Department of Physics, University of Colorado Boulder, Boulder, Colorado 80309, USA
[4]Materials Science and Engineering Program, University of Colorado Boulder, Boulder, Colorado 80309, USA
[*]juliet.gopinath@colorado.edu

Abstract: This study demonstrates the fabrication and evaluation of a monolithic electrowetting prism with a minimized electrode gap. The electrically tunable prism is capable of two-dimensional beam steering of approximately ±4 degrees under voltage differentials up to ±15 V. The main innovation lies in reducing the electrode gap to 30 μm, accomplished using direct write laser lithography on three dimensional substrates. Through simulations and experimental validation, we show that reducing the gap between electrodes to 30 μm enables the transmission of a 1.2 mm diameter beam with negligible impact on imaging quality. The improved imaging quality makes electrowetting prisms an attractive option for future advancements in optical scanning technologies.

1. Introduction

Beam steering technologies are necessary for various optical systems such as light detection and ranging (LiDAR) [1–6], optical coherence tomography (OCT) [7–11], laser scanning microscopy [12–20], and optical displays [21–23]. Depending on the application, the beam scanning element can be mechanical or non-mechanical. Common mechanical systems employ microelectromechanical systems (MEMS) mirrors [17–20] or galvanometric mirrors [16,24]. Non-mechanical scanners such as spatial light modulators [25,26], liquid lens-prism elements [27–30], electro-optic scanners [31] and liquid crystals [32–35] are another option. Although a multitude of scanning technologies are available, the choices become scarce when size, weight, speed and power constrained environments are considered. For example, to perform brain imaging in awake animals, using a head-mounted microscope, the system weight requirement is ≤ 4 g for mice, and the size of the entire package should be less than $\sim 10 \times 10$ mm^2 [20,36,37]. In this case, an attractive solution is electrowetting tunable optics. The advantages of electrowetting-based optical devices over conventional adaptive optics are evident; these fluidic devices eliminate the need for mechanical moving parts, ensuring compactness and easy integration into small-scale optical systems. Operating under low power, they have been demonstrated to function at kHz speeds, a notable contrast to other non-mechanical alternatives. Furthermore, electrowetting-based optics offer the distinct advantage of operation in transmission instead of reflection, allowing for simplified optical design compared to reflective beam steering elements, such as MEMS-based mirrors. Overall, these devices stand out for their mechanical simplicity, compactness, low-voltage operation, high-speed capabilities, and transmissive operation. Electrowetting tunable lenses have already been implemented in microscopy [36,38,39], miniaturized zoom lenses [40,41], microlens arrays [42–44] and endoscopes [45]. Meanwhile, electrowetting prisms have shown

#536641 https://doi.org/10.1364/OE.536641
Journal © 2024 Received 15 Jul 2024; revised 24 Aug 2024; accepted 25 Aug 2024; published 26 Sep 2024

Optics EXPRESS

promise for LiDAR [4,46,47], laser scanning microscopy [16], solar tracking [48] and wavefront control [49–51].

A review of literature analyzing head-mounted two-photon microscopes designed for *in-vivo* mice brain imaging reveals a trend: MEMS mirrors, typically ranging from 0.8-1.2 mm in mirror diameter, are often used as scanning elements [18,20,36,37]. If the benefits of electrowetting scanners are to be realized for these systems, the electrowetting element must be able to scan a beam of ~1.2 mm diameter while preserving imaging quality. The main challenge is the optical performance of multi-electrode electrowetting devices. The presence of individually addressable sidewall electrodes necessitates an electrode gap that tends to distort liquid-liquid interfaces. In this work, we present a novel method for fabrication of electrowetting tunable prisms. Utilizing direct write laser lithography on three dimensional substrates, we demonstrate an electrowetting-based prism scanner capable of large scanning angles ($> \pm 4°$), with the ability to transmit a > 1 mm diameter beam with negligible effect on the imaging quality of the optical system, due to the small electrode gap achieved using direct laser write lithography. In this manner, the advantages of a transmissive beam scanning element can be fully harnessed, simplifying optical designs and reducing microscope footprints.

2. Electrowetting background

Electrowetting uses an applied electric field to manipulate the wettability of a solid surface. This allows the contact angle of a polar liquid droplet to be modified by applying a voltage across the droplet and an electrode separated by a dielectric layer [52–56]. The Lippmann-Young equation determines the contact angle based on applied electric potential,

$$\cos(\theta) = \cos(\theta_0) + \frac{\epsilon_d \epsilon_0}{2t\gamma} V^2 \tag{1}$$

where θ is the contact angle due to applied voltage V, θ_0 is the zero voltage contact angle, ϵ_d is the dielectric permittivity, t is the dielectric thickness, and γ is the interfacial surface energy.

We leverage this effect by functionalizing cylindrical glass tubes with an electrode layer (Indium Tin Oxide), a dielectric layer (Parylene HT), and a hydrophobic layer (Cytop, used to increase the initial contact angle). The functionalized glass tube is then attached to a bottom optical ground window and filled with immiscible polar and non-polar liquids of contrasting refractive indices. We use deionized (DI) water as the polar liquid and 1-phenyl-1-cyclohexene (PCH) as the non-polar liquid, selected for their large refractive index contrast ($\Delta n = 0.17$), fast actuation speeds, and excellent density matching ($\Delta\rho < 0.01$ g/mL) [57–60]. We further increase our control over the liquid interface by including multiple, individually addressable sidewall electrodes [16,61], as shown in Fig. 1(a). In this case, the electrowetting-controlled liquid-solid contact angle is localized at the electrode, resulting in the ability to actuate the liquid interface in an asymmetric manner. A three-dimensional rendering of a four electrode device is shown in Fig. 1(a). When all four electrodes are biased to V_{flat} (the voltage corresponding to a 90° contact angle), a voltage differential, V_{scan}, can be applied to opposing electrodes, such that $V_1 = V_{flat} - V_{scan}$ and $V_2 = V_{flat} + V_{scan}$, resulting in $\theta_1 > \theta_2$, as shown by the cross-sectional representation in Fig. 1(b). In this manner, we are able to create electrowetting based two-dimensional beam scanning prisms.

While multi-electrode devices allow for the necessary asymmetric control of the liquid interface required for beam steering, this comes at the cost of unactuated regions in the liquid-liquid interface where the electrode gaps are present. In the ideal, yet nonphysical, case where there is no electrode gap in a four-electrode electrowetting prism, the contact angle can be defined at four arcs along the device circumference (each having an enclosed angle of 90°). However, when electrode gaps are present, the gaps between electrodes must remain at the experimentally determined zero-voltage contact angle of 173° [57].

Optics EXPRESS

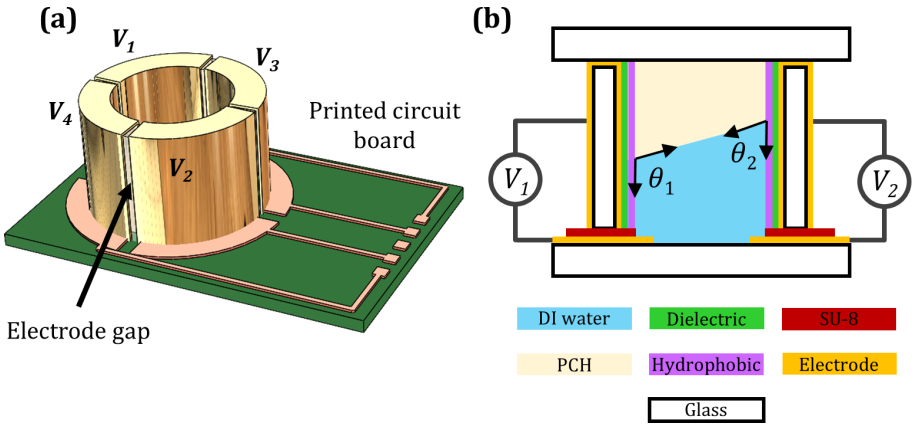

Fig. 1. (a) Three-dimensional rendering of a four-electrode electrowetting prism. The electrodes are labelled with V_1 through V_4, and the electrode gap is exaggerated. The final device can be attached to a custom printed circuit board for electrical connection. (b) Cross-sectional image of an electrowetting prism showing voltage application on the vertical electrode and bottom ground electrode. Parylene HT serves as the dielectric and Cytop as the hydrophobic layer. At the voltage V_{flat}, the contact angle of the liquid interface with the device wall is 90°. A voltage differential V_{scan} can be applied to opposing electrodes, resulting in a tilted liquid interface.

2.1. *Effect of electrode gap size on the liquid interface*

To understand how the electrode gap (unactuated region) affects the morphology of the liquid-liquid interface, we carried out numerical simulations to find the equilibrium surface profile of our electrowetting prisms with two different electrode gap sizes. The geometric configuration used in our simulation is based on the physical properties of our devices. The devices are constructed in 4 mm inner diameter, 5 mm tall glass tubes and filled with equal volumes of DI water and PCH. The size of the gap between electrodes is varied from 30 μm (this work) to 400 μm corresponding to our previous work [57,62].

We solved the interfacial surface profile between the two liquids using the Young-Laplace equation [63–65]. The model is based on the energy minimization principle and solves for the steady-state surface, and does not account for transient effects. By solving the Young-Laplace equation, we can describe the equilibrium shape of a liquid-liquid interface for a given boundary condition set by the electrode voltages. The partial differential equation (PDE) toolbox in MATLAB is used to solve the equation for the geometry shown in Fig. 2(a). The steady-state contact angles were experimentally determined to be 173° with no applied voltage [57] and Eq. (1) is used to relate the applied voltage to the liquid-solid contact angle at each electrode as a boundary condition in the Young-Laplace equation:

$$\nu \cdot \left(\nabla u / \sqrt{1 + |\nabla u|^2} \right) = \cos\theta \tag{2}$$

where $u(x, y)$ is the liquid-liquid interface surface, ν is the unit exterior normal, and θ is the angle between the surface and the cylinder wall. The liquid-liquid surface profile is controlled by geometry at the boundaries (voltages on the electrodes). This method has been previously validated by comparing to time dependent three-dimensional computational fluid dynamics (CFD) carried out in COMSOL (Laminar two-phase flow module) [49,62]. In this work, we extend the capability of the simulation by including the effect of the electrode gap, where the liquid interface contact angle remains at the initial contact angle of 173°. Figure 2(b) and (c) show the simulated liquid-liquid interface when all four electrodes are biased to a 90° contact

Optics EXPRESS

angle, for a device with a 30 and 400 μm electrode gap size, respectively. In both cases illustrated, the ideal interface would be a flat liquid-liquid interface, but the discontinuity of the contact angle caused by the electrode gap causes distortions in the liquid-liquid interface. The effect of the electrode gap is clearly exacerbated by the larger electrode gap (400 μm). While some distortions remain with a smaller electrode gap of 30 μm, they are clearly reduced, as evidenced by the order of magnitude decrease in variation of the surface. We have also simulated the steady-state beam steering conditions for both electrode gap sizes. Here all electrodes are first biased to V_{flat} (90° contact angle), followed by a voltage differential ($\pm V_{scan}$) applied to a pair of opposing electrodes resulting in a deflection of the liquid-liquid interface. The simulated liquid-liquid interfaces corresponding to a 10 V differential are shown in Fig. 2(d) and (e).

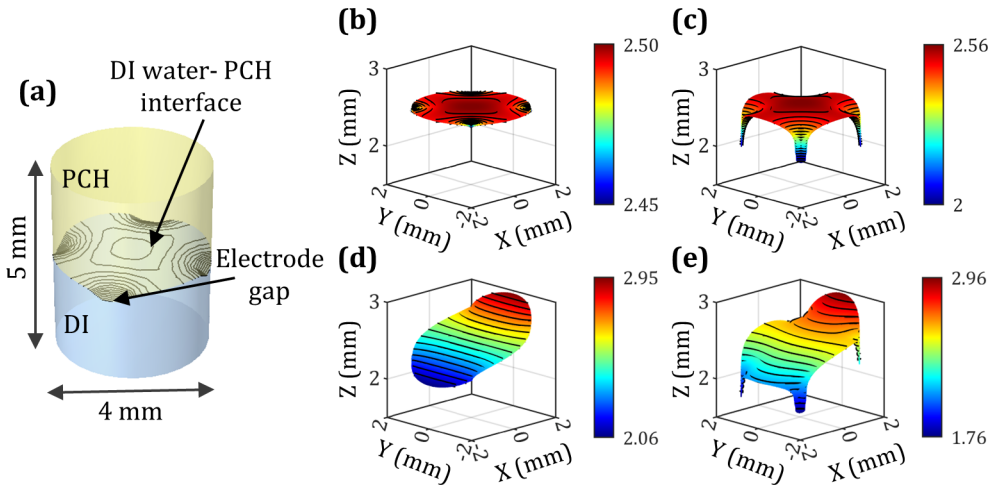

Fig. 2. (a) Full simulation geometry for the 4-electrode device. The electrode gap can be seen to cause distortions to the steady-state interface profile. (b) Simulation of the 4-electrode device after applying 78 V (90° contact angle) to all electrodes, while keeping the 30 μm electrode gaps at 0 V. (c) Simulation of the 4-electrode device after biasing all electrodes to 90° contact angle, while keeping the 400 μm electrode gaps at 173°. (d) Simulation of the 4-electrode device when a 10 V differential is applied to opposing electrodes. The electrode separation is 30 μm. (e) Simulated liquid-liquid interface for a 400 μm electrode gap device with a 10 V differential applied on opposing electrodes.

Reducing the electrode gap to 30 μm diminishes undesirable effects from the electrode gap near the center of the device, bringing it closer to the ideal scenario of a perfectly flat liquid-liquid interface. To illustrate, we analyze the interfacial surface profile along a line connecting the centers of the electrode gaps and compare it with a line profile directly between the electrode centers. Figures 3(a) and (c) depict the lines on the surfaces corresponding to the profiles presented in Figs. 3(b) and (d) for the devices with 30 μm and 400 μm electrode gaps, respectively. In the case of the 30 μm electrode gap device, the line profiles exhibit similarity with slight curvature evident in the 45° profile. Conversely, the line profiles for the device with a larger 400 μm electrode gap display significant differences in the two directions. Along the 0° line, there is some curvature, while the 45° line exhibits substantial curvature, demonstrating a range of approximately 500 microns from the edge to the center of the profile. This highlights the inherent challenge posed by the physical constraint of an electrode gap; the surface profile consistently varies every 45° for a standard four-electrode device. Still, the reduced electrode gap results in an order of magnitude reduction in root-mean-square deviation between the 0 and 45° surface profiles compared to the 400 μm electrode gap.

Optics EXPRESS

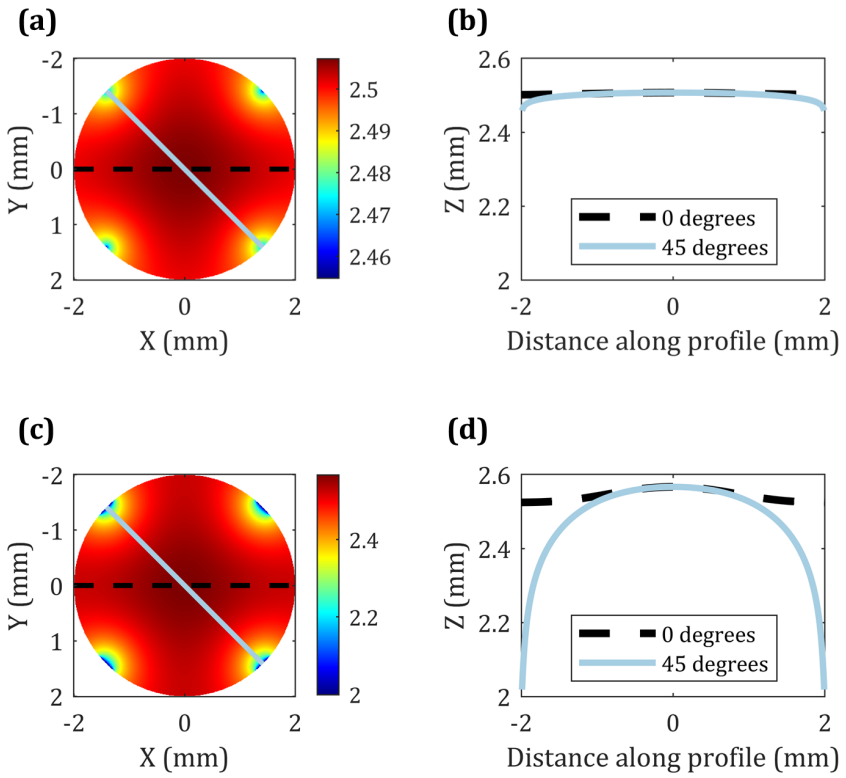

Fig. 3. (a) Simulated interfacial surface profile for an electrowetting prism actuated to 90° contact angle at the electrodes while the gaps remain at 173° contact angle. The gap size is 30 μm. (b) Line profiles of simulated liquid-liquid interface for a 30 μm electrode gap device. (c) Simulated interfacial surface profile for an electrowetting prism having 400 μm electrode gaps. (d) Line profiles of simulated liquid-liquid interface for a 400 μm electrode gap device.

The liquid-liquid interfaces extracted from the Young-Laplace solution are imported in simulation to the optical system design software, Ansys Zemax OpticStudio, using the Zemax grid sag function. The ray tracing simulation setup is shown in Fig. 4(a). Here, an input beam is transmitted through the simulated electrowetting devices of varying electrode gap size. A paraxial lens is used to check the beam quality at the image plane. The size of the input beam is varied from 0.25 to 3.25 mm. One measure of optical quality is the Strehl ratio, which compares the peak intensity of the actual point-spread function (PSF) of an optical system to the ideal PSF [66]. A Strehl ratio of 1 indicates a perfect optical system, where all the rays are focused perfectly into a single point, while a Strehl ratio of above 0.8 is generally considered good imaging quality [67]. Figure 4(b) shows the Strehl ratio as a function of the input aperture for a 30 and 400 μm electrode gap electrowetting device where all electrodes are biased to 90° contact angle. While the Strehl ratio for both begins close to one for 0.25 mm input beam diameter, a rapid decrease for the 400 μm electrode gap device is evident as the input beam diameter is increased. The Strehl ratio for the 30 μm electrode gap device also decreases with increasing beam size, but can be seen to remain above 0.8 until the input beam diameters becomes larger than 2 mm. The Huygens PSF calculated using Zemax for a 1.5 mm beam transmitted through the electrowetting device can be seen in Figs. 4(c) and (d) for a 30 and 400 μm electrode gap device, respectively. The sidelobes evident in Fig. 4(d) arise from the diffraction based PSF calculation in which a grid

Optics EXPRESS

of rays is traced from the source to the imaging plane. A coherent sum for all rays is performed at every point in the image space resulting in a diffraction pattern due to the curvature of the 400 μm gap surface. In Fig. 4(c), the sidelobes are not evident as the 30 μm gap surface tends to be much more flat, leading to a higher peak value. The Strehl ratio remains at 0.98 for the 30 μm electrode gap device, while it diminishes to 0.22 for the 400 μm electrode gap device, despite both starting at a Strehl ratio above 0.99 for a 0.25 mm input aperture.

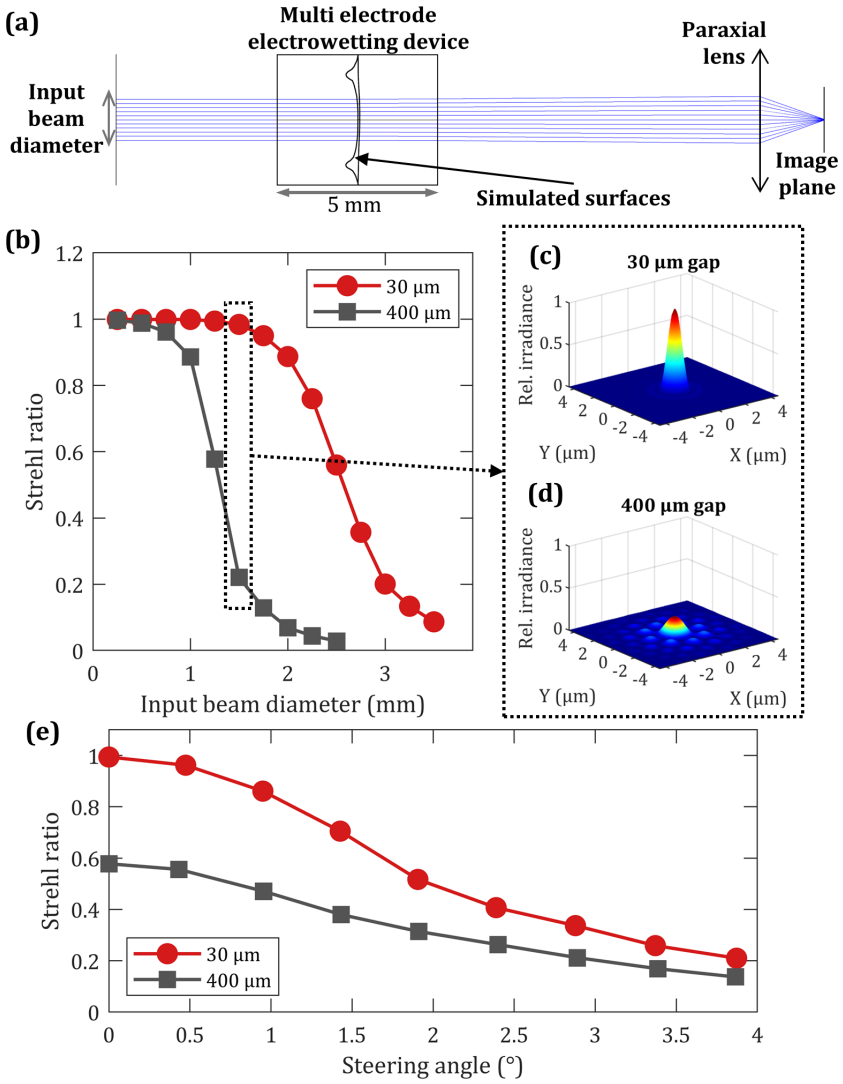

Fig. 4. (a) Schematic optical design for measuring the optical quality of electrowetting prism devices with different electrode gap sizes. The liquid-liquid interface is imported into Zemax through the Zemax grid sag function. Ray tracing is performed on the imported surfaces. The corresponding Strehl ratio after imaging with a paraxial lens is evaluated at the image plane. (b) Strehl ratio as a function of input beam diameter for electrowetting prisms with a 30 μm (dots) and 400 μm (square) electrode gap when all electrodes are biased to V_{flat}. (c),(d) Point-spread functions for a 1.5 mm beam transmitted through a 30 and 400 μm electrode gap electrowetting devices. (e) Strehl ratio as a function of beam steering angle for electrowetting prisms with a 30 μm (dots) and 400 μm (square) electrode gap. The input beam diameter is 1.25 mm.

Optics EXPRESS

The off-axis performance of both devices is also evaluated in Fig. 4(e). This is done by importing the simulated surfaces with voltage differentials applied between opposing electrodes, leading to a one-dimensional deflection of the passing beam. For a 1.25 mm input beam diameter, the 30 μm gap device is seen to consistently produce a higher Strehl ratio than a device having a 400 μm electrode gap, which has a low Strehl ratio regardless of beam steering angle. Although the Strehl ratio falls below 0.8 at slightly above 1° of beam steering angle for the 30 μm electrode gap device, there remains a path forward to implementation of these devices in high performance optical systems. Kopp *et al.* performed a study noting that the curvature of the tilted liquid-liquid interface decreases with increasing electrodes [68], though they did not account for the effect of the electrode gap in their analysis. We expect that the off-axis performance would similarly improve with more sidewall electrodes here.

3. Device fabrication

Previously, monolithic electrowetting based tunable prisms have been fabricated in cylindrical containers at millimeter scale using Kapton tape [61] or 3D printed masks [29,57,62] to pattern the electrode gap on the sidewall. While these methods are reliable, they suffer from large electrode separations, ~1 mm in the case of Kapton masks, and ~400 μm in the case of 3D printed shadow masks (the comparison used in the preceding sections). Non-cylindrical designs have also been demonstrated by fabricating planar substrates which are then assembled into rectangular containers [46,69,70], but the sharp corners and rectangular geometry that result from this method lead to poor optical surfaces and suffer from complex fabrication. Other designs have demonstrated high quality optical surfaces by using 2D lithography to fabricate addressing electrodes on thin polyimide substrates which are then rolled and inserted into cylindrical glass tubes [51,68,71]. While this leads to high optical quality surfaces, the multi-piece design can make device packaging difficult compared with a monolithic layout. In this work, we present a method for fabricating monolithic four electrode electrowetting prisms in cylindrical containers using direct write lithography on the 3D substrate. The new method results in an order of magnitude smaller electrode gap size compared to Kapton or 3D printed masks (30 μm vs. ~ 400 μm), improving the optical quality of the device.

3.1. Direct laser write lithography system

One of the most prevalent lithography methods is contact lithography [72], wherein a pattern is exposed onto photoresists using a mask. Although highly repeatable and fast, this method is not well-suited for non-planar substrates. An alternative for writing photoresist patterns is through maskless lithography methods such as ion beam, electron beam, or direct laser write lithography. In direct laser write lithography, a laser source scans across the photoresist. This method offers small resolution limits, determined by the objective used and wavelength of the laser source, while maintaining fair throughput and relatively lower cost compared to other maskless methods [73–75]. A simple, cost-effective approach for achieving direct laser write lithography for SU-8 patterning involves using commonly available 405 nm laser diodes and motorized stages to scan either the light source or the substrate [73,76,77].

We present a direct-write lithography system capable of patterning on three-dimensional substrates. The system employs a 405 nm laser diode collimated to ~1 mm full width at half maximum (FWHM) diameter and focused through a 10X, 0.28 Numerical Aperture (NA), 200 mm working distance objective. Figure 5 illustrates the exposure system, configured to focus UV light on the inner tube wall of an SU-8 coated glass tube. To achieve an electrode separation spanning the entire tube, the focal point must be scanned. Utilizing a motorized stage, we scan the coated tube vertically, followed by a 90-degree rotation and repetition of the process. This results in developed ~30 μm wide sections of SU-8 spanning the tube's height. Figure 5(b) shows the processed and developed SU-8 on the inner wall of a glass tube. This SU-8 section serves as

Optics EXPRESS

a mask when the tube is sputter-coated with the electrode material, and an SU-8 lift-off process is executed to create the functionalized glass tube, as detailed in the following section.

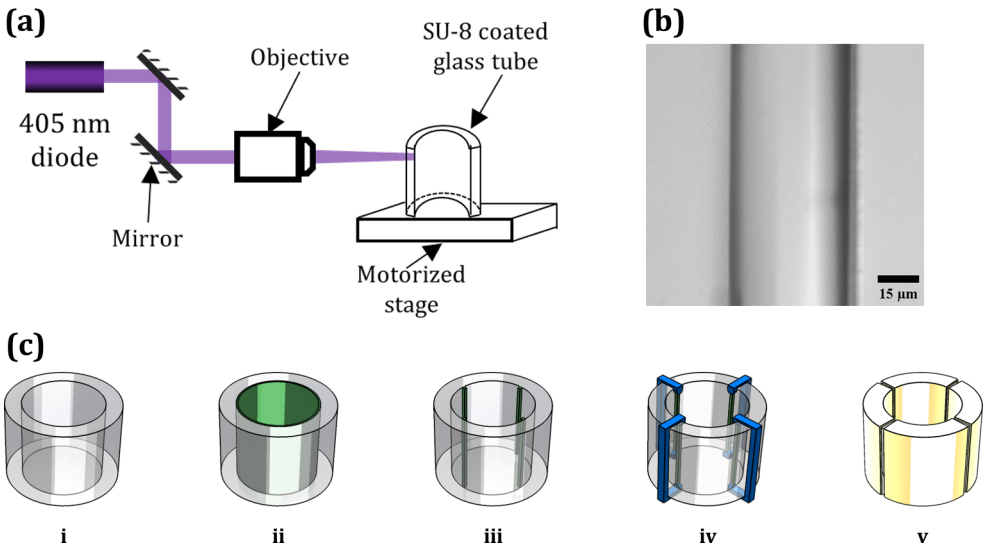

Fig. 5. (a) Diagram of the laser lithography system. A 405 nm laser diode is collimated and passed through an objective, the focus of which is placed on the inner wall of an SU-8 coated glass tube. The focused spot is then scanned along the height of the glass tube by using a motorized stage. (b) Optical microscope image of an exposed and developed layer of SU-8 on the inner sidewall of a cylindrical glass tube. The developed region can be seen to be ~30 μm wide. (c) Fabrication process for electrowetting prisms: i) Prepare a clean glass tube. ii) Coat inner sidewall with SU-8. iii) Pattern and develop SU-8. iv) Install shadow mask on tube to mask outer sidewall and inner tube edges. v) Sputter deposit electrode and perform SU-8 lift-off.

3.2. *Electrowetting prism fabrication*

We begin by cleaning the substrate, a 4 mm inner diameter, 5 mm tall glass tube, using acetone and isopropyl alcohol. After drying with compressed nitrogen, a layer of SU-8 3010 is coated on the inner sidewall using a polyurethane foam swab and the tube is soft baked at 65°C for 5 minutes. The uniformity of the SU-8 layer was not explicitly quantified in this study due to its location on the interior surface of a cylindrical substrate. However, as the layer serves as a lift-off layer, minor variations in thickness will not impact the device's final functionality. Next, the SU-8 is exposed using the custom-built laser lithography system described above. The SU-8 coated inner sidewall of the tube is placed at the focal spot of the objective, and a motorized stage is used to move the tube vertically at 100 μm/s, resulting in an exposure dosage of 980 J/cm^2. The tube is then rotated 90°, and the exposure process is repeated three additional times, resulting in four lines of exposed SU-8 at 90° from one another. The total write time is ~3.3 minutes per device. Following exposure, a post-exposure bake is performed at 95° C for 6 minutes. The exposed SU-8 is then submerged completely in SU-8 developer for 5 minutes and agitated gently. At this stage, the patterned and developed SU-8 remaining on the inner sidewall of the substrate will serve as a mask when the electrode material is deposited.

The adhesion of SU-8 at the sharp corners near the tube rim is inconsistent, and a mask for the outside of the glass tube must be made to maintain electrical isolation of the electrodes. To solve both issues, a single 3D printed shadow mask spanning the tube's height at the outer diameter

Optics EXPRESS

and protruding 500 μm inside at the top and bottom is used, as shown in Fig. 5(c). Indium tin oxide (ITO), used as the vertical side electrode, was deposited uniformly along the inner and outer sidewalls of the tube using direct current sputtering at 60 W and an argon pressure of 15 mTorr. The shadow mask was removed, and an SU-8 lift-off was performed by submerging the coated tubes in 1-Methyl-2-pyrrolidone (NMP) heated to 60° C for 1 hour, followed by a sonication bath of NMP at room temperature for 15 minutes to prevent redepositing of the swelled SU-8. Finally, the tubes are rinsed with isopropyl alcohol, and the conductivity of the ITO vertical electrodes was increased by annealing at 300 ° C for one hour. Prior to depositing the necessary dielectric and hydrophobic layers, the glass tube is cleaned and the entirety of the outer diameter is masked with Kapton tape to preserve electrode contact on the outside of the tube after the dielectric deposition. Parylene HT (3 μm) is deposited in a vapor-phase, commercially (Specialty Coating Systems). The tubes are then dip-coated in a 10 wt.% Cytop and cured at 185° C for one hour, creating the hydrophobic layer. The optical ground window is fabricated on a glass substrate by adding annular patterned electrodes, lithographically patterned using NR-7 photoresist. The ground electrode, consisting of 10 nm Ti/200 nm Au, was sputtered onto the wafer, and excess ground electrode material is removed through a lift-off process in an acetone bath to create the clear aperture. SU-8 3050 (~50 μm) was then deposited and lithographically patterned as an electrical insulation layer between the vertical electrodes and ground electrode. The functionalized glass tube is next aligned to the clear aperture of the patterned ground window and the two are epoxy bonded together. A custom printed circuit board is subsequently attached to the assembled electrowetting prism with silver epoxy to facilitate electrical connection to the driving electronics.

4. Experimental methods and results

Following device fabrication, we characterize the performance of our electrowetting tunable prisms. One crucial metric is the voltage differential to beam steering angle characterization, which we measure experimentally. We also quantitatively characterize the optical quality of our devices by measuring the PSF when collimated beams of varied diameters are transmitted through our device and imaged using an aspheric lens.

4.1. Scan angle characterization

We employ a 633 nm laser diode collimated to a 0.5 mm ($1/e^2$) diameter to characterize the voltage differential to beam steering angle characteristics of our device. The laser beam traverses the electrowetting scanning device and is directed onto a CMOS camera positioned 20 mm from the liquid meniscus of the electrowetting device. The steering angle is calculated using the distance from the liquid meniscus to the CMOS sensor and the lateral beam displacement. The experimental setup is illustrated in Fig. 6(a). Prism-based beam steering is achieved by actuating all electrodes to the voltage corresponding to a 90° contact angle with the sidewall, denoted as V_{flat}. Subsequently, a voltage difference (V_{scan}) can be introduced to opposing electrodes for linear scanning along either axis. The device is actuated for V_{scan} values in 1 V increments up to 15 V in each orthogonal direction. The measurement is taken after the device has reached its steady-state beam steering angle which takes approximately 100 ms for the device geometry and liquids used [57].

The results, depicted in Fig. 6(b), demonstrate consistent steering angles of approximately ~4 degrees in either direction, in line with the predicted scan angle. The predicted scan angle is extracted by measuring the beam steering angle when the simulated surfaces are imported into Zemax. Deviation of the experimental and predicted steering angles could be attributed to minor optical misalignment in the experimental setup as well as fabrication errors.

Optics EXPRESS

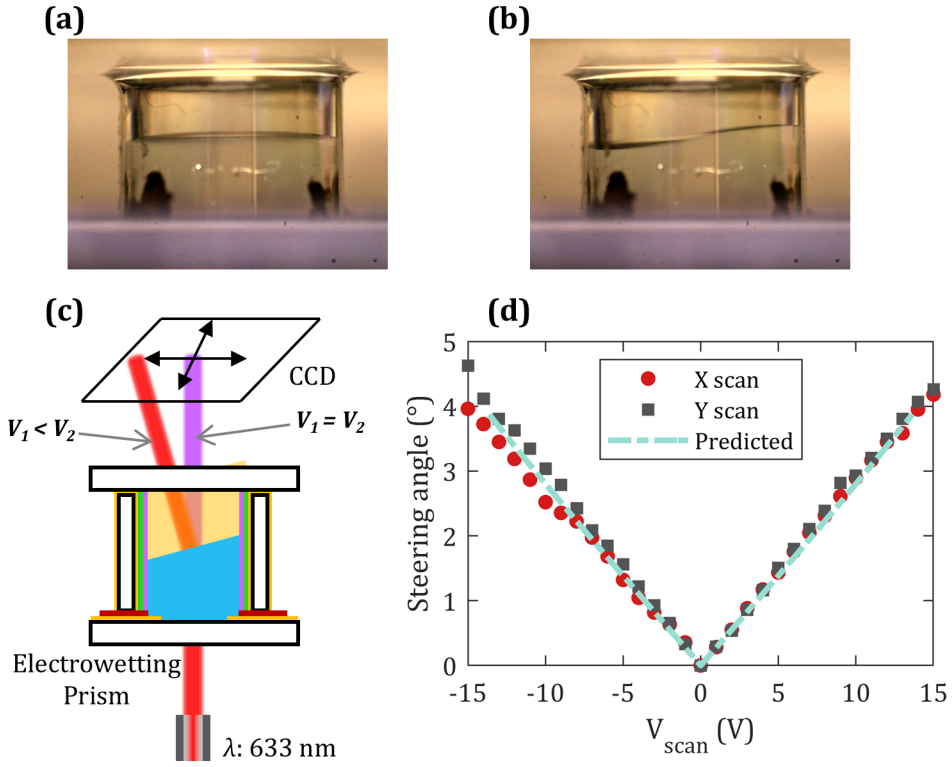

Fig. 6. (a) Side image of the electrowetting tunable prism with all electrodes biased to a 90° contact angle. (b) Side image of the electrowetting tunable prism with a voltage differential of 10 V applied between the left and right electrodes. (c) Schematic of the experimental setup for characterizing electrowetting prism scan angle. A 633 nm laser diode is collimated to a 0.5 mm diameter ($1/e^2$) and passed through the center of a four-electrode electrowetting prism with all electrodes biased to V_{flat}. V_1 and V_2 are the voltages placed on opposing electrodes and equal to $V_{flat} \pm V_{scan}$. The beam centroid displacement is measured on a camera sensor as V_{scan} is swept to ±15 V. (d) Beam steering angle as a function of the voltage differential applied to opposing electrodes, measured by beam centroid displacement on a CCD. The electrowetting prisms exhibit ~±4° steering angle with V_{scan} = ±15 V. Some slight asymmetry is observed between positive and negative scans, as well as in the x- and y-directions, attributed to minor optical misalignment and fabrication errors.

4.2. *Imaging quality characterization*

As we aim to employ electrowetting-based prisms as scanning elements in imaging systems, the aberrations introduced by the prism scanner itself must be reduced. As discussed earlier, simulations suggest that reducing the electrode gap size increases the useful aperture, approximating an ideal liquid interface. If a 1.2 mm diameter beam can be transmitted through our devices without significantly impacting imaging quality, the advantages of a transmissive electrowetting based beam scanning element can be fully harnessed, a step towards simplifying optical designs and reducing microscope footprints.

Simulation results in Sec. 2.1 predict nearly diffraction-limited optical performance when using the central 1.2 mm diameter of the 30 μm electrode gap device aperture, a significant improvement over a similar device with a 400 μm electrode gap. We experimentally confirm the optical quality of our devices by collimating a 633 nm laser diode to 1.2, 2.0, and 2.4 mm diameters ($1/e^2$) and passing the beam through an electrowetting prism with all electrodes biased

Optics EXPRESS

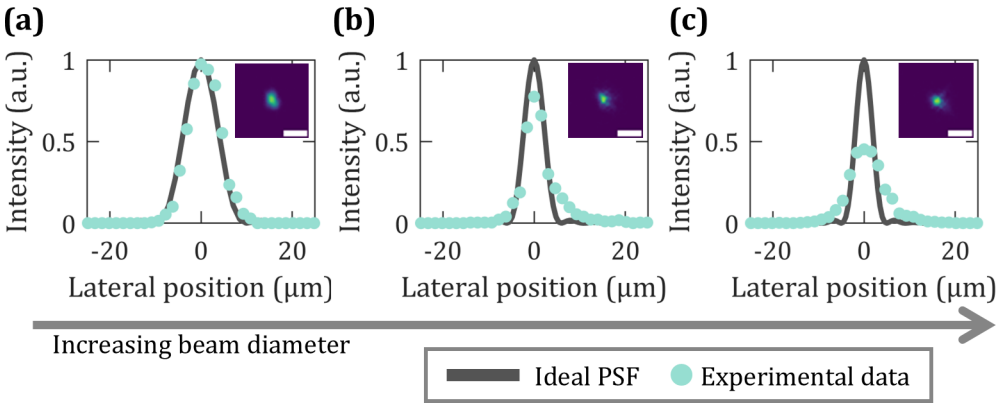

Fig. 7. Normalized intensity cross-sections of each focused spot. The gray line represents the ideal PSF as calculated using Zemax, the blue dots represent the experimental PSF after the beam is transmitted through a 30 μm electrode gap electrowetting device for (a) 1.2 mm input beam diameter, (b) 2.0 mm input beam diameter, and (c) 2.4 mm input beam diameter. The insets show the focal spot as measured on a CCD. The scale bar is 25 μm.

to a 90° contact angle. The transmitted beam is focused onto a CCD camera sensor using an aspheric lens (15.3 mm focal length, 0.16 NA). The cross section of the point-spread function is then evaluated and normalized such that the integral of the experimental data matches the integral of the ideal point-spread function. Following this, the ratio of the peak intensities, I, can be used to experimentally determine the Strehl ratio [66], S, as

$$S = \frac{I_{PSF}^{(real)}(0,0)}{I_{PSF}^{(ideal)}(0,0)}. \tag{3}$$

The normalized point-spread function cross sections can be seen in Fig. 7(a)-(c) for a 1.2, 2.0, and 2.4 mm input beam diameter, respectively. The ideal PSF is simulated using a Zemax model of the imaging asphere used in the experiment and the input beam diameter with no electrowetting element in the path. It can be seen that as the input beam diameter increases, the experimental PSF deviates further from the ideal, with the peak intensity falling off, due to the larger sampling of the liquid-liquid interface of the electrowetting device causing aberrations. The measured Strehl ratio varies from 0.97 for a 1.2 mm input beam diameter to 0.78 for a 2 mm beam and 0.45 for a 2.4 mm beam, matching well with the simulation predicted Strehl ratios (Fig. 4). Furthermore, the experimentally demonstrated ability of our devices to transmit up to a 2 mm beam with negligible impact on imaging quality positions them as viable beam steering elements in miniaturized microscopes for *in-vivo* brain imaging in freely behaving mice, with potential applications in other imaging and optical systems.

5. Conclusion

In summary, this work has successfully demonstrated the fabrication and characterization of a one-piece electrowetting prism with a minimal electrode gap, aiming to improve imaging quality for miniaturized optical systems. The electrowetting prism exhibits consistent two-dimensional beam steering with approximately ±4 degrees for voltage differentials up to ±15 V. The key innovation lies in minimizing the electrode gap to enhance optical performance, a crucial factor for applications in miniaturized laser scanning microscopes. Through simulations and experimental validation, we have shown that reducing the electrode gap to 30 μm significantly improves the optical quality of electrowetting-based tunable prisms, enabling the transmission of a 1.2 mm

Optics EXPRESS

beam with negligible impact on imaging quality. This advancement positions electrowetting optics as promising components for compact and efficient optical systems, especially in the context of miniaturized microscopes for applications such as *in-vivo* brain imaging in freely behaving mice. The small footprint, simplicity, and enhanced imaging quality make electrowetting prisms a compelling choice for future developments in optical scanning technologies.

Funding. Office of Naval Research (N00014-20-1-2087); National Institutes of Health (R01NS123665, UF1NS116241); National Science Foundation (1919148, 1926668, 1926676); University of Colorado (Anschutz-Boulder Nexus Seed Grant).

Acknowledgments. The authors acknowledge the use of Colorado Shared Instrumentation in Nanofabrication and Characterization (COSINC) and JILA fabrication facilities at the University of Colorado Boulder. We thank Dr. Catherine Saladrigas and Samuel Gilinsky for fruitful discussions. Publication of this article was funded by the University of Colorado Boulder Libraries Open Access Fund.

Disclosures. The authors declare no conflicts of interest.

Data availability. Data underlying the results presented in this paper are not publicly available at this time but may be obtained from the authors upon reasonable request.

References

1. R. T. H. Collis, "Lidar," Appl. Opt. **9**(8), 1782 (1970).
2. G. W. Kattawar and G. N. Plass, "Time of Flight Lidar Measurements as an Ocean Probe," Appl. Opt. **11**(3), 662 (1972).
3. T. Raj, F. H. Hashim, A. B. Huddin, *et al.*, "A Survey on LiDAR Scanning Mechanisms," Electronics **9**(5), 741 (2020).
4. M. Zohrabi, W. Y. Lim, R. H. Cormack, *et al.*, "Lidar system with nonmechanical electrowetting-based wide-angle beam steering," Opt. Express **27**(4), 4404 (2019).
5. C. Niclass, K. Ito, M. Soga, *et al.*, "Design and characterization of a 256x64-pixel single-photon imager in CMOS for a MEMS-based laser scanning time-of-flight sensor," Opt. Express **20**(11), 11863 (2012).
6. D. Wang, C. Watkins, and H. Xie, "MEMS Mirrors for LiDAR: A Review," Micromachines **11**(5), 456 (2020).
7. G. Song, E. T. Jelly, K. K. Chu, *et al.*, "A review of low-cost and portable optical coherence tomography," Prog. Biomed. Eng. **3**(3), 032002 (2021).
8. R. A. Leitgeb, "En face optical coherence tomography: a technology review [Invited]," Biomed. Opt. Express **10**(5), 2177 (2019).
9. A. G. Podoleanu, "Optical coherence tomography," The Br. J. Radiol. **78**(935), 976–988 (2005).
10. Y. Pan, H. Xie, and G. K. Fedder, "Endoscopic optical coherence tomography based on a microelectromechanical mirror," Opt. Lett. **26**(24), 1966 (2001).
11. J. Sun, S. Guo, L. Wu, *et al.*, "3D In Vivo optical coherence tomography based on a low-voltage, large-scan-range 2D MEMS mirror," Opt. Express **18**(12), 12065 (2010).
12. F. Helmchen and W. Denk, "Deep tissue two-photon microscopy," Nat. Methods **2**(12), 932–940 (2005).
13. K. Svoboda and R. Yasuda, "Principles of Two-Photon Excitation Microscopy and Its Applications to Neuroscience," Neuron **50**(6), 823–839 (2006).
14. W. Alford, R. VanderNeut, and V. Zaleckas, "Laser scanning microscopy," Proc. IEEE **70**(6), 641–651 (1982).
15. B. V. R. Tata and B. Raj, "Confocal laser scanning microscopy: Applications in material science and technology," Bull. Mater. Sci. **21**(4), 263–278 (1998).
16. O. D. Supekar, B. N. Ozbay, M. Zohrabi, *et al.*, "Two-photon laser scanning microscopy with electrowetting-based prism scanning," Biomed. Opt. Express **8**(12), 5412 (2017).
17. C. Zhao, Y. Zhu, D. Zhang, *et al.*, "Millimeter field-of-view miniature two-photon microscopy for brain imaging in freely moving mice," Opt. Express **31**(20), 32925 (2023).
18. W. Zong, H. A. Obenhaus, E. R. Skytøen, *et al.*, "Large-scale two-photon calcium imaging in freely moving mice," Cell **185**(7), 1240–1256.e30 (2022).
19. W. Piyawattanametha, E. D. Cocker, L. D. Burns, *et al.*, "In vivo brain imaging using a portable 29 g two-photon microscope based on a microelectromechanical systems scanning mirror," Opt. Lett. **34**(15), 2309 (2009).
20. W. Zong, R. Wu, M. Li, *et al.*, "Fast high-resolution miniature two-photon microscopy for brain imaging in freely behaving mice," Nat. Methods **14**(7), 713–719 (2017).
21. M.-H. Kiang, O. Solgaard, K. Y. Lau, *et al.*, "Polysilicon optical microscanners for laser scanning displays," Sens. Actuators, A **70**(1-2), 195–199 (1998).
22. J. Bae, Y.-S. Choi, K. Choi, *et al.*, "Arrayed beam steering device for advanced 3D displays," (San Francisco, California, USA, 2013), p. 86160H.
23. J. C. Heikenfeld, N. R. Smith, B. Sun, *et al.*, "Flat electrowetting optics and displays," (San Jose, CA, 2008), p. 688705.

Optics EXPRESS

24. B. Jaeggi, B. Neuenschwander, U. Hunziker, *et al.*, "Ultra-high-precision surface structuring by synchronizing a galvo scanner with an ultra-short-pulsed laser system in MOPA arrangement," (San Francisco, California, USA, 2012), p. 82430K.
25. E. Haellstig, J. Stigwall, M. Lindgren, *et al.*, "Laser beam steering and tracking using a liquid crystal spatial light modulator," (Orlando, FL, 2003), p. 13.
26. Q. Niu and C. Wang, "High precision beam steering using a liquid crystal spatial light modulator," Opt. Quantum Electron. **51**(6), 180 (2019).
27. V. Mai and H. Kim, "Non-Mechanical Beam Steering and Adaptive Beam Control Using Variable Focus Lenses for Free-Space Optical Communications," J. Lightwave Technol. **39**(24), 7600–7608 (2021).
28. Y. Cheng, J. Cao, and Q. Hao, "Optical beam steering using liquid-based devices," Opt. Lasers Eng. **146**, 106700 (2021).
29. M. Zohrabi, R. H. Cormack, and J. T. Gopinath, "Wide-angle nonmechanical beam steering using liquid lenses," Opt. Express **24**(21), 23798 (2016).
30. Y.-J. Lin, K.-M. Chen, and S.-T. Wu, "Broadband and polarization-independent beam steering using dielectrophoresis-tilted prism," Opt. Express **17**(10), 8651 (2009).
31. G. Römer and P. Bechtold, "Electro-optic and Acousto-optic Laser Beam Scanners," Phys. Procedia **56**, 29–39 (2014).
32. Z. He, F. Gou, R. Chen, *et al.*, "Liquid Crystal Beam Steering Devices: Principles, Recent Advances, and Future Developments," Crystals **9**(6), 292 (2019).
33. D. P. Resler, D. S. Hobbs, R. C. Sharp, *et al.*, "High-efficiency liquid-crystal optical phased-array beam steering," Opt. Lett. **21**(9), 689 (1996).
34. Z. He, K. Yin, and S.-T. Wu, "Miniature planar telescopes for efficient, wide-angle, high-precision beam steering," Light: Sci. Appl. **10**(1), 134 (2021).
35. Y. Li, Z. Luo, and S.-T. Wu, "High-Precision Beam Angle Expander Based on Polymeric Liquid Crystal Polarization Lenses for LiDAR Applications," Crystals **12**(3), 349 (2022).
36. B. N. Ozbay, J. T. Losacco, R. Cormack, *et al.*, "Miniaturized fiber-coupled confocal fluorescence microscope with an electrowetting variable focus lens using no moving parts," Opt. Lett. **40**(11), 2553 (2015).
37. T. Liu, M. Rajadhyaksha, and D. L. Dickensheets, "MEMS-in-the-lens architecture for a miniature high-NA laser scanning microscope," Light: Sci. Appl. **8**(1), 59 (2019).
38. F.-L. Kuang, R.-Y. Yuan, Q.-H. Wang, *et al.*, "Large zooming range adaptive microscope employing tunable objective and eyepiece," Sci. Rep. **10**(1), 14644 (2020).
39. S. D. Gilinsky, D. N. Jung, G. L. Futia, *et al.*, "Tunable liquid lens for three-photon excitation microscopy," Biomed. Opt. Express **15**(5), 3285 (2024).
40. Y.-C. Fang, C.-M. Tsai, and C.-L. Chung, "A study of optical design and optimization of zoom optics with liquid lenses through modified genetic algorithm," Opt. Express **19**(17), 16291 (2011).
41. L. Li, D. Wang, C. Liu, *et al.*, "Zoom microscope objective using electrowetting lenses," Opt. Express **24**(3), 2931 (2016).
42. C. U. Murade, D. van der Ende, and F. Mugele, "High speed adaptive liquid microlens array," Opt. Express **20**(16), 18180 (2012).
43. C. Kim, D. Shin, G. Koo, *et al.*, "Fabrication of an electrowetting liquid microlens array for a focus tunable integral imaging system," Opt. Lett. **45**(2), 511 (2020).
44. S. D. Gilinsky, M. Zohrabi, W. Y. Lim, *et al.*, "Fabrication and characterization of a two-dimensional individually addressable electrowetting microlens array," Opt. Express **31**(19), 30550 (2023).
45. M. E. Pawlowski, S. Shrestha, J. Park, *et al.*, "Miniature, minimally invasive, tunable endoscope for investigation of the middle ear," Biomed. Opt. Express **6**(6), 2246 (2015).
46. J. Lee, J. Lee, and Y. H. Won, "Beam steering and forming in compact electrowetting prism array with separate electrode control," OSA Continuum **4**(9), 2400 (2021).
47. N. R. Smith, D. C. Abeysinghe, J. W. Haus, *et al.*, "Agile wide-angle beam steering with electrowetting microprisms," Opt. Express **14**(14), 6557 (2006).
48. J. Cheng, S. Park, and C.-L. Chen, "Optofluidic solar concentrators using electrowetting tracking: Concept, design, and characterization," Sol. Energy **89**, 152–161 (2013).
49. M. Zohrabi, R. H. Cormack, C. Mccullough, *et al.*, "Numerical analysis of wavefront aberration correction using multielectrode electrowetting-based devices," Opt. Express **25**(25), 31451 (2017).
50. P. Zhao, D. Sauter, and H. Zappe, "Tunable fluidic lens with a dynamic high-order aberration control," Appl. Opt. **60**(18), 5302 (2021).
51. D. Sauter, M. Sieben, P. Zhao, *et al.*, "Simultaneous beam steering and shaping using a single-interface optofluidic component," J. Optical Microsystems **1**(04), 044002 (2021).
52. B. Berge and J. Peseux, "Variable focal lens controlled by an external voltage: An application of electrowetting," The Eur. Phys. J. E **3**(2), 159–163 (2000).
53. F. Mugele and J.-C. Baret, "Electrowetting: from basics to applications," J. Phys.: Condens. Matter **17**(28), R705–R774 (2005).
54. B. H. W. Hendriks, S. Kuiper, M. A. J. VAN As, *et al.*, "Electrowetting-Based Variable-Focus Lens for Miniature Systems," Opt. Rev. **12**(3), 255–259 (2005).

Optics EXPRESS

55. H. Ren and S. Wu, *Introduction to Adaptive Lenses* (Wiley, 2012), 1st ed.
56. J.-C. Baret, M. M. J. Decré, and F. Mugele, "Self-Excited Drop Oscillations in Electrowetting," Langmuir **23**(9), 5173–5179 (2007).
57. W. Y. Lim, O. D. Supekar, M. Zohrabi, *et al.*, "Liquid Combination with High Refractive Index Contrast and Fast Scanning Speeds for Electrowetting Adaptive Optics," Langmuir **34**(48), 14511–14518 (2018).
58. O. D. Supekar, M. Zohrabi, J. T. Gopinath, *et al.*, "Enhanced Response Time of Electrowetting Lenses with Shaped Input Voltage Functions," Langmuir **33**(19), 4863–4869 (2017).
59. E. J. Miscles, W. Y. Lim, O. D. Supekar, *et al.*, "Axisymmetrical resonance modes in an electrowetting optical lens," Appl. Phys. Lett. **122**(20), 201106 (2023).
60. P. Zhao, Y. Li, and H. Zappe, "Accelerated electrowetting-based tunable fluidic lenses," Opt. Express **29**(10), 15733 (2021).
61. S. Terrab, A. M. Watson, C. Roath, *et al.*, "Adaptive electrowetting lens-prism element," Opt. Express **23**(20), 25838 (2015).
62. W. Y. Lim, M. Zohrabi, J. T. Gopinath, *et al.*, "Calibration and Characteristics of an Electrowetting Laser Scanner," IEEE Sens. J. **20**(7), 3496–3503 (2020).
63. R. Finn, *Equilibrium Capillary Surfaces*, vol. 284 of Grundlehren der mathematischen Wissenschaften (Springer, 1986).
64. S.-L. Lee and C.-F. Yang, "Numerical simulation for meniscus shape and optical performance of a MEMS-based liquid micro-lens," Opt. Express **16**(24), 19995 (2008).
65. T. Sarpkaya, "Vorticity, Free Surface, and Surfactants," Annu. Rev. Fluid Mech. **28**(1), 83–128 (1996).
66. H. Gross, *Aberration Theory and Correction of Optical Systems*, vol. 3 (Wiley-VCH Verlag, 2007).
67. M. Born, E. Wolf, A. B. Bhatia, *et al.*, *Principles of Optics: Electromagnetic Theory of Propagation, Interference and Diffraction of Light* (Cambridge University Press, 1999), 7th ed.
68. D. Kopp, L. Lehmann, and H. Zappe, "Optofluidic laser scanner based on a rotating liquid prism," Appl. Opt. **55**(9), 2136 (2016).
69. J. Lee and Y. H. Won, "Achromatic doublet electrowetting prism array for beam steering device in foveated display," Opt. Express **30**(2), 2078 (2022).
70. S. Tun, Y.-R. Zhao, J.-B. Xu, *et al.*, "Dual interface trapezium liquid prism with beam steering function," Opt. Express **32**(3), 3394 (2024).
71. D. Kopp and H. Zappe, "Tubular astigmatism-tunable fluidic lens," Opt. Lett. **41**(12), 2735 (2016).
72. M. Wang, ed., *Lithography* (InTech, 2010).
73. C. A. Rothenbach and M. C. Gupta, "High resolution, low cost laser lithography using a Blu-ray optical head assembly," Opt. Lasers Eng. **50**(6), 900–904 (2012).
74. S. Heiskanen, Z. Geng, J. Mastomäki, *et al.*, "Nanofabrication on 2D and 3D Topography via Positive-Tone Direct-Write Laser Lithography," Adv. Eng. Mater. **22**(2), 1901290 (2020).
75. A. C. Sullivan, M. W. Grabowski, and R. R. McLeod, "Three-dimensional direct-write lithography into photopolymer," Appl. Opt. **46**(3), 295 (2007).
76. Y. Cheong, W. Lim, S. Lee, *et al.*, "405 nm laser processing of thin SU-8 polymer film," Optik **127**(4), 1651–1655 (2016).
77. P. Mueller, M. Thiel, and M. Wegener, "3D direct laser writing using a 405 nm diode laser," Opt. Lett. **39**(24), 6847 (2014).